Reconfigurable Vacuum Sample Holder for Through-Silicon Microscopy and Laser-Assisted Bonding

Aleksandr Andreevich Vlasov, *Member, IEEE*, Topi Uusitalo, Heikki Virtanen, Jukka Viheriälä, and Mircea Guina, *Member, IEEE*

***Abstract*—Current development trends concerning miniaturizing of electronics and photonics systems are aiming at assembly and 3D co-integration of a broad range of technologies including MEMS, microfluidics, wafer level optics, multilayered structures with through-silicon vias connection, and silicon photonics. Modern integration processes impose severe requirements on the design and functionality of research and assembly setups and their parts. In this work we demonstrate a simple, reliable, and cost-effective reconfigurable vacuum sample holder that ensures fast reconfiguration for electronic and photonic integration using laser assisted bonding (LAB) processes. The design is compatible with IR through-silicon microscopy with top and bottom irradiation/illumination architectures, which makes this concept instrumental for a large variety of research, assembly, lithography, and wafer bonding setups.**

***Index Terms*—Assembly processes, infrared imaging, infrared microscopy, laser-assisted bonding, photonic integration, silicon devices, silicon photonics, through-silicon vision.**

I. Introduction

The annual growth of data transfer rates linked to digitalization of the world economy, for example in the form of artificial intelligence, *IoT*, and large-scale machine-to-machine communication, requires a continued development of information and communication technology (ICT) infrastructure, microelectronics, and photonic devices. In 2018 the overall IP traffic was predicted to grow up to 396 exabytes (EB) per month by the end of 2022 [1], including monthly mobile network data traffic of around 108 EB [2]. The underlying technology is largely enabled by miniaturization of electronics and photonics, which allows to reach a tremendous shrinking of modules to a chip the size of a thumbnail [4], [5], [6]. Similar trends, leading to convergence of electronics and photonics technology platforms are visible in other application areas, including integrated sensors for wearable devices, or advanced solid-state coherent LIDAR technology.

Manuscript received 11 July 2023; revised 1 August 2023; accepted 3 August 2023. Date of publication 7 August 2023; date of current version 23 August 2023. This work was supported in part by Business Finland through Project Photonic Integrated Circuits for Industrial Applications under Grant 44761/31/2020 and in part by the Academy of Finland through Photonics Flagship Program Photonics Research and Innovation under Grant 320168. *(Corresponding author: Aleksandr Andreevich Vlasov.)*

The authors are with the Optoelectronics Research Centre, Physics Unit, Tampere University, 33720 Tampere, Finland (e-mail: aleksandr.vlasov@tuni.fi).

Digital Object Identifier 10.1109/JPHOT.2023.3302404

Established approaches for microelectronics-photonics co-integration processes include mass-reflow (MR) and thermo-compression bonding (TCB, intended to override the thermally induced warpage by applying the uniform pressure). Yet, there is a growing need to develop more advanced tools addressing precise alignment of photonics components, faster assembly process, and in general reproducibility and higher production rate. To this end, Laser-Assisted Bonding (LAB), which is known to be much faster than classical TCB and MR processes, is expected to meet the strict requirements of precise bonding owing to negligible thermo-induced stress and warpage of the bonded surfaces (up to 3–4 times lower) [6], [7]. This aspect is very relevant for photonic integration processes, as warpage leads to optical axes misalignment. It is likely that as photonic wire bonding (PWB) technology matures [8], this issue becomes less critical, but for now it is a strong limitation. Yet another advantage is the fact that LAB can rely on solder surface tension-driven self-alignment [9], which can help to achieve the best performance for integration [7], [10].

II. Laser-Assisted Bonding: The Short Review

The LAB is a process of surface-to-surface bonding mediated by laser-induced surface heating. Generally, photons will couple into the electronic or vibrational states in the material depending on their energy. It will stimulate excited states in a material during irradiation, and then transfer energy to lattice phonons. This is the typical energy absorption mechanism, and it causes a material response in the form of temperature increase. Furthermore, the mass density of material, the specific heat, thermal conductivity, and irradiation time should be also considered for the laser heating mechanism and its simulation. Building on the benefits of laser beaming, heat energy is localized very precisely and used for melting the solder or even the bonded substrates themselves. LAB is already used in a large variety of fields, such as microelectronics, photonics, MEMS, biomedical technology etc. [11], [12], [13], [14], [15], [16], [17]. The laser wavelength is chosen according to the absorption spectra of the bonded surfaces where light-to-heat conversion takes place [18]. For silicon-related bonding processes the wavelengths around 975–980 nm and 1475 nm are typically used [18], [19], [20], [21], [22], [23], [24], [25], [26], [27], [28], [29], [30], [31], [32]. In the first case silicon is used as a light absorbing, heat integrating and

This work is licensed under a Creative Commons Attribution 4.0 License. For more information, see https://creativecommons.org/licenses/by/4.0/

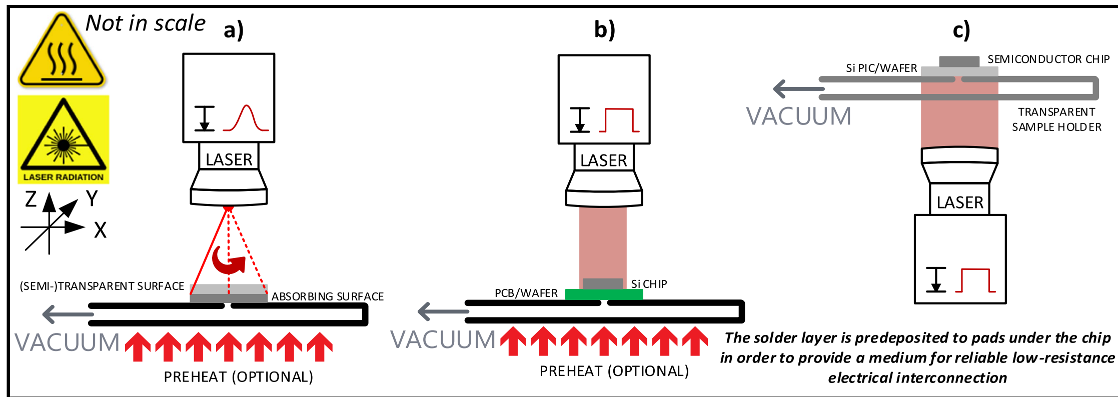

Fig. 1. LAB processes: (a)–Gaussian beam profile (in scanning mode), (b)–uniform beam profile (top irradiation), (c)–uniform beam profile (bottom irradiation).

conducting media, whereas in the second case the laser radiation meets silicon transparency window and light-to-heat conversion occurs directly on the bonding pads [31].

According to the laser beam profile used, LAB processes could be divided into Gaussian (Fig. 1(a)) [11], [12], [13], [14], [15], [16], [17] and uniform ("top-hat") beam processes (Fig. 1(b)–(c) [18], [19], [20], [21], [22], [23], [24], [25], [26], [27], [28], [29], [30], [31], [32]. Usually, LAB processes with a Gaussian beam profile are used to create maximal power density at the bonded surfaces. It is used in such applications as biomedical instrumentation, high-temperature electronics packaging, MEMS, silicon-to-glass, silicon-to-sapphire, glass-to-glass, hermetic wafer-to-wafer bonding, dissimilar materials bonding etc. [11], [12], [13], [14], [15], [16], [17]. As a general guideline, the laser is used in a surface scanning mode (in *XY* plane according to the coordinate system shown in Fig. 1). The important process parameters are the laser power, scanning velocity, scanning path, and repetition rate. This type of laser assembly processes usually requires sophisticated and complex physical models for numerical simulation [17]. Typical process parameters include a spot diameter of 25 μm–1 mm, scanning speed of 0.1–0.5 mm/s, fluence of 2–10 J/cm^2, and repetition rate up to 20 kHz [9], [10], [11], [12], [13], [14]. As an example process, laser light source from the Nd:YAG Q-switched laser processing system with a wavelength of 355 nm, a spot diameter of 25 μm with the combination of parameters 0.1 mm/s speed, 0.3 W per pulse, and 12 kHz rate was used to bond 80 μm thick single crystal quartz chips to silicon substrates. In this case intermediate layers of Cr, Au and Sn, with the composition of Au:Sn set close to eutectic ratio of 80:20 wt.% were used to provide high bond strength of over 15 MPa at rapid processing rates [16].

LAB processes with a Gaussian beam profile could be also used for implementation of fluxless soldering technique for the attachment of optoelectronic components to silicon submounts by laser soldering of gold-coated indium solder pads. By keeping the Nd:YAG 1064 nm 200 μm spot laser irradiation time of 60 ms per pad (through silicon submount), and employing a soldering sequence that minimizes the formation of indium oxide, it is possible to solder without flux or the need of an inert atmosphere. The method was demonstrated on a high-speed data link consisting of a laser, an external modulator, and a laser back facet detector attached to a silicon submount [12]. It was also demonstrated that the soldering sequence also affects the bonding reliability and quality [12].

LAB processes with a uniform beam profile are usually using a beam homogenizer for transformation from Gaussian to a "top-hat" shape with dimensions close to the dimensions of bonded surfaces (Fig. 1(b) and (c) [19], [20], [21], [22], [23], [24], [25], [26], [27], [28], [29], [30], [31], [32]. In that way, bonded surfaces are heated evenly, and all the pads are soldered at the same time. The usage of a Gaussian laser beam for those purposes is reported to be the reason for device cracking and bond failures. Open-circuit issues are related to the areas under the tails of the beam receiving insufficient laser power, whereas short-circuit issues and surface destruction are related to excessive laser power in the center area [20]. The adjustable profile beam homogenizers with aspect ratio typically ranging from 1:1 to 1:18 and beam width of up to 135 mm are commercially available. The most crucial parameters of the processes include the laser power, surfaces areas and thicknesses, irradiation time and the number of soldering pads. Typical process parameters are: laser power of 30–150 W, irradiation time – below 1 s, heating area – up to 55 $\times$ 55 mm [18], [19], [20], [21], [22], [23], [24], [25], [26], [27], [28], [29], [30]. As an example process, a 980 nm laser was used for bonding of 6 $\times$ 6 $\times$ 0.18 mm silicon chip with 23 $\times$ 12 μm copper bump pillars (40–80 μm pitch) covered with Sn3.0%Ag0.5%Cu solder with melting temperature of $\sim$220 °C. The process consists of two stages: 0.4 s @ 120 W/cm^2 ("ramp-up") and 0.8 s @ 74 W/cm^2 ("dwell") [29].

Moreover, it was also reported the possibility of producing the 3D integrated multilayer devices using through-silicon vias (TSV) by the use of LAB not only in a layer-by-layer mode, but also in a multilayer collective bonding regime [30]. The maximum number of stacked 15 $\times$ 15 mm silicon chips that can be collectively integrated using non-conductive paste (NCP) with a 3 s @ 150 W LAB process (980 nm) was observed to be six [30]. The results of the collective LAB process indicate that all the six layers were successfully bonded [30].

Most of microelectronics-related LAB processes reported, independently from beam profile used, due to large dimensions of

PCBs, and therefore, large heat capacity of the system, require a preheating of the bonding stage (chuck, sample holder) with temperature of +70°–+110 °C, which could be achieved by the usage of electrical heaters [29] or high-power halogen lamps [12].

We should also note that laser assisted processes can be used for de-bonding. Laser-Assisted de-Bonding (LAdB) is a reliable method for removing faulty devices on 3D and multi-die chip packages [21]. Owing to the properties of intermetallic compounds (IMC) formed during LAB, de-bonding usually requires more heat energy [19]. LAB and LAdB are highly selective and topical methods for efficient and sustainable repairing of faulty chip packages and other semiconductor devices [21].

In the LAB processes for microelectronic integration, silicon chips are usually bonded to printed-circuit boards (PCBs), so the laser usually is placed above the assembly (Fig. 1(b)), and could be combined with vacuum pick-up-tool [25]. As for photonic integration processes, when semiconductor chips are bonded to silicon photonic integration circuits (PICs) or wafers, laser is usually placed below the assembly (Fig. 1(c)) [29]. In microelectronics, the similar through-PCB irradiation architecture is also known as Reverse LAB (R-LAB) [32].

For temperature control and feedback, a thermocouple [22], [30], a pyrometer [24], [26], or an IR camera (thermal imager) [21], [27], [29] could be used. Thermal imager allows to control the temperature distribution among several points or the whole bonding surface.

Traditionally, common methods for investigating the quality of the bonded interfaces include post-bond X-ray inspection [33], [34], [35] and through-silicon infrared (IR) microscopy, which exploits silicon transparency at wavelengths longer than 1 μm. Through-silicon imaging is beneficial for semiconductor components alignment evaluation and monitoring the bonding process in real-time [36], [37]. The most typical image sensor types used for modern through-silicon IR microscopy, allowing the detection of longer wavelengths, are *InGaAs* [31], [38], [39], *Ge* [38], or *black silicon (bSi)* [40] cameras. To enable the possibility of through-silicon vision, the sample must be finely polished; surface roughness has a large impact on the vision quality and the value of 0.5 μm is reported to be excessively high for this purpose [31]. The reported accuracy of the through-silicon vision-based alignment is within ±300 nm range [31].

Post-bond electrical (forward voltage or bond resistance) and optical (peak wavelength, power) parameters control can be used to evaluate the bonding quality of LEDs and micro-LEDs (μLEDs) [25], [33]. It is shown, that with a decrease bonding energy, the forward voltage also tends to decrease [25]. Also, a red-shift in LED wavelengths is attributed to higher bonding laser energies [25]. Typical measured contact resistance after LAB was in the range of hundredths of an Ohm [33].

In general, the imaging and monitoring steps require development of specialized sample holders that are customized to specific illumination configuration and the laser delivery architecture. Usually, samples and/or wafers are held in place by vacuum sample holders (chucks), as this enables fast on-off switching capabilities and provides low contamination risks. The number of holes for the chuck vacuum and their location are usually component-specific [41], [42]. Component placement is usually achieved by using pick-and-place tools [43], whereas wafer positioning is achieved by mounting a chuck on motorized stages [44]. Often chucks are combined with preheating units [41], [45]. Some of processes require transparent designs of a chuck: UV-transparent [45], THz-transparent [47] and IR-transparent [31] chucks were reported. Furthermore, most of research applications require custom chuck design [47], [48], [49]. Also, for precise microscopy applications chuck and the setup itself may be mounted on a solid rigid basis with the use of properly designed vibration isolation system to suppress environmental noise [50], [51]. As a general conclusion summarizing the development needs for advanced LAB processes applied to electronic and photonic integration processes, it is necessary to have a reconfigurable vacuum design of the chuck, transparent both for LAB and IR microscopy optical radiation sources [31], [39], and allowing the use of different types of pick-and-place tools.

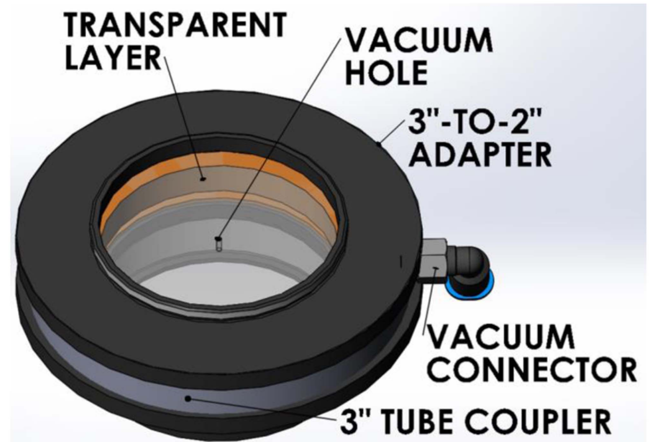

Fig. 2. Explanatory drawing for the proposed vacuum sample holder design.

To this end, we demonstrate a simple, reliable, and cost-effective reconfigurable vacuum sample holder design. It is mostly based on inexpensive commercially available components to ensure fast reconfiguration of the holder to new electronic and photonic integration based on LAB. Also, it is compatible with IR through-silicon microscopy with top and bottom irradiation (or illumination) architecture. This makes this concept applicable to a large variety of research, assembly, lithography, and wafer bonding setups.

III. Vacuum Sample Holder Design Concept

The schematic of the design concept is presented in Fig. 2. The design relies on forming an airtight cavity from two layers of transparent materials. The top-layer has one or several holes for holding the wafer(s) and/or component(s) using vacuum. The cavity is connected to a vacuum line with a standard connector. The frame for these transparent layers is made from standard 3”-to-2” lens tube adapters, connected with a standard 3” externally threaded lens tube coupler with a vacuum connector installed to its side surface. To form the cavity, there is a spacer between

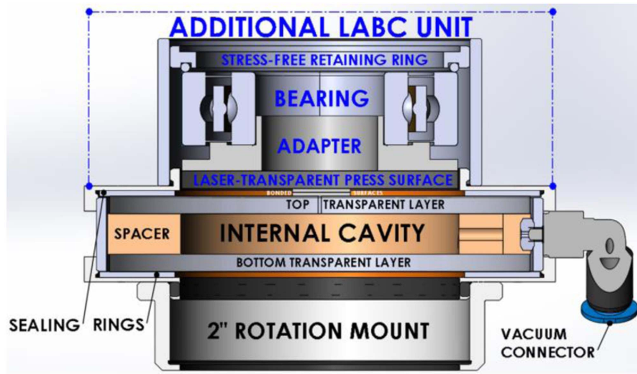

Fig. 3. Explanatory drawing for the proposed vacuum sample holder design: The simplified cross-section.

the transparent layers with a side hole aligned with the vacuum connector. The space between the transparent layers and the inner surfaces of 3”-to-2” adapters are sealed with custom flat rubber O-rings. Also, several independently controlled cavities with individual vacuum connectors could be created for work with different independent chips/wafers.

This design of the chuck is for bottom-illuminated reflected light microscopy with observation area diameter of 2”, the vacuum holes configuration of which could be easily changed by replacement of top layer according to the type, dimensions, and number of samples under observation. The first prototypes realized have a single vacuum hole with a diameter of 1 mm in the center of top surface to accommodate the dimensions of the test samples.

The development and production of devices for specific applications, such as biomedical instrumentation, high-temperature electronics packaging, MEMS, silicon-to-glass, silicon-to-sapphire, glass-to-glass, hermetic wafer-to-wafer bonding and some other encapsulation technologies (Fig. 1(a)), require the use of laser-assisted bonding with compression (LABC) processes, when the bonded surfaces are additionally compressed with 0.3–3 MPa pressure during laser irradiation [11], [12], [13], [14], [15], [16]. To satisfy these conditions, the proposed design may be equipped with an additional unit, which consists of a 2” lens tube with a precise rotating component (shown as a bearing), which is mechanically connected (e.g., bonded, glued, welded, soldered etc.) to laser-transparent press surface via an adaptor and could be equipped with its own vacuum cavity for holding the upper bonded surface (not shown). This unit converts its rotation to a compressing force acting on bonded surfaces without their displacement or any transmission of rotation. The simplified explanatory drawing for the design concept is presented in Fig. 3.

To ensure the required sub-μm alignment accuracy, the sample holder design must consider all potential displacement sources of the bonded surfaces, i.e., rotation and linear movements.

The source of rotational displacement is the potential transition of rotation by the rotating component (around the Z axis *(Rz)* according to the coordinate system in Fig. 1). The bonded surfaces are free from rotational displacement if the following condition is met:

$$M_{rot} \ll M_{bnd} \tag{1}$$

where M_{bnd} – is the total sum of frictional moments between bonded surfaces, top transparent layer, and press surface (depended on the materials, their dimensions, desired compression force and vacuum holding force of a chuck), and M_{rot} – is the total frictional moment of a rotating component (bearing). Here all moments are in *N·m*.

According to the known mathematical model, the bearing friction is not constant and depends on certain tribological phenomena that occur in the lubricant film between the rolling elements, raceways, and cages [52]. To calculate the total frictional moment in a rolling bearing, the following sources and their tribological effects must be taken into account [52]:

$$M_{rot} = M_{rr} + M_{ss} + M_{seal} + M_{drag} \tag{2}$$

where M_{rr} – is the rolling frictional moment, M_{ss} – is the sliding frictional moment, M_{seal} – is the frictional moment of seals and M_{drag} – is the frictional moment of drag losses, churning, splashing etc. These frictional moments are strongly depended on the bearing type, its configuration, tolerances, clearance, and mechanical alignment degree [52]. High tolerances and misalignment generally increase the sliding frictional moment. High operation temperatures and/or high rotation speed might reduce internal bearing clearance, which can increase friction. However, if we consider friction as a function of speed, in this application rotating component operates at boundary layer lubrication condition, in which only the asperities carry the load, and so friction between the moving surfaces is highest of the entire bearing operating range [52]. Nevertheless, the usage of precise properly lubricated with the recommended amount of grease bearing with low tolerances could satisfy (1), and, therefore, provide the required range of compressing force and alignment accuracy [52]. Moreover, in this application the axial compression load theoretically may become an issue, but as the required static compression force is low (typically, in the range of units of kilograms for bonded surfaces from 5 × 5 mm to 2” wafers [11], [12], [13], [14], [15], [16]) the impact of this factor on friction is also low. For higher loads tapered bearings could be used.

The potential source of linear displacements (in *XY* plane according to the coordinate system in Fig. 1) is the mutual non-parallelism of press surface ant top transparent layer planes at the initial moment of interaction. This problem can be solved by manufacturing the bearing-to-press-surface adapter from the elastic material, which allows small rotations along *Y* and *X* axes (*Ry* and *Rx* according to the coordinate system in Fig. 1), excluding the rotation around the *Z* axis *(Rz)*. In this case, the diameter of the press surface should be chosen in order to prevent any interaction with any components of a setup, except from the bonded surfaces. Besides, the spring constant of the elastic material of the adapter will form a compensating force for backlashes of the bearing and the thread, which are able to cause a hysteresis in compression force.

To suppress the environmental noise and vibrations impacts, the sample holder is mounted on a solid rigid basis with the use

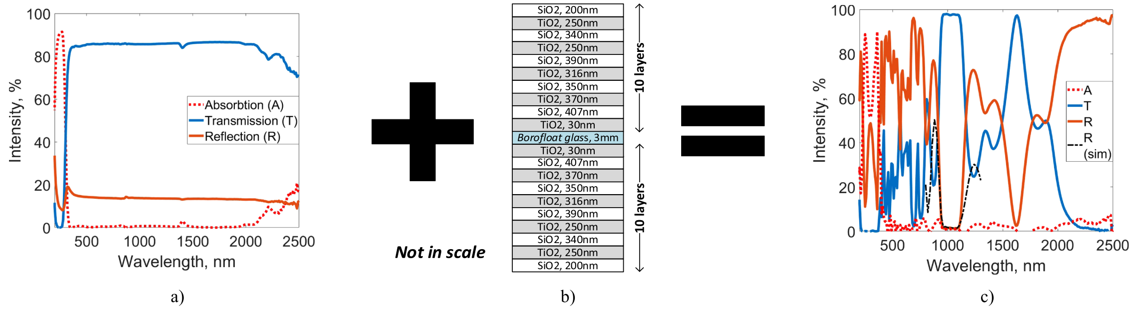

Fig. 4. Optical spectra for *Borofloat* glass-based sample holder: (a)-Without AR-coatings (ARCs), (b)–ARCs structure, (c)-with ARCs.

of properly designed vibration isolation system [50], [51]. Positioning and alignment of the components are carried out using precise vacuum pick-up tool, mounted on a 6-axis manipulator with sub-μm movement precision. Position, rotation, and tilt measurements of the components are performed using machine-vision system (including through-silicon alignment [40]) and scanning optical distance sensors with sub-μm measurement precision.

To avoid heat damage, melting and deformation of the surfaces in LAB applications (which leads to components misalignment and contamination), as well as to ensure the necessary transmission range, in the first prototypes of the proposed design 3 mm thick *Borofloat* glass sheets are used as transparent layers. Other materials with high light durability, low thermal expansion, and suitable transmission spectrum, such as *Sapphire* [31], could also be used. Preferable processing type is waterjet cutting technique, as it does not produce a heat affected zone and therefore the material is free from thermal and deformation stresses, leading to fine and clean cut [53].

For LAB and through-silicon IR microscopy applications in the field of silicon photonics, both surfaces of transparent layers are covered with 10-layer TiO_2/SiO_2 AR coatings (ARCs). The coatings were designed to minimize bonding laser and IR vision illumination source optical losses due to reflectance and absorbance in the wavelength range of 950–1100 nm. The coatings were evaporated by ion beam sputtering.

In this process an ion beam was steered towards different metal plates (targets). The ion beam contained accelerated oxygen ions that reacted with the metal plates, causing metal oxide vapor beam that was directed on the transparent layers. In-situ transmission monitoring was used to ensure that the designed optical thickness of the material layers was obtained. The overall thickness of each ARC is below 2.5 μm and the surface roughness of the transparent layers after ion beam sputtering process is comparable to the initial surface roughness of the *Borofloat* glass. Thus, the ARCs application in this sense could be considered as the uniform thickness increase of the transparent layers in a micrometer range, which, in turns, means that if sealing rings are used and threads are sufficiently tightened, AR coatings do not affect the hermitization level of the sample holder.

The resulting transmittance (T), absorbance (A), and reflectance (R) spectra of sample holder, as well as ARC structure and reflection numerical simulation results (sim), with reference to uncoated sample holder, are presented in Fig. 4. The data was obtained using *PerkinElmer Lambda 1050* spectrophotometer setup with a scanning step of 10 nm.

As it can be seen, the AR-coated *Borofloat* glass sample holder itself acts as an optical bandpass filter with maximum reflectance of 1.2% and absorbance of 1.1% in the wavelength range of 950–1100 nm. Its transmission in this wavelength range exceeds 97%, which is on average 12% higher than in case of PMMA-based (Poly(methyl methacrylate)) sample holder (83–85%), whereas reflectance is about 14 times lower (14% for PMMA) [40]. Optionally, if the process requires a preheating of the bonding stage [12], [29], i.e., in case of a wafer-level assembly, an additional absorbing layer could be attached to the upper glass to enable light-induced preheating capability with bottom or top illumination source with wavelength outside the 950–1100 nm range. Also, according to the absorption spectrum in Fig. 4(c) UV-LEDs, UV- or halogen lamps can be used with existing ARCs, providing the light-to-preheat conversion efficiency of up to 90% [12].

Three prototypes of the proposed design were fabricated, which had different materials for the spacer between transparent layers and the sealing rings. For the Prototype 1, the spacer was 3D printed of flexible filament with density of 1.6 kg/m^3 and hardness of 98 Shore A and sealing rings were made of 0.8 mm thick rubber with hardness of 72 Shore M. For Prototype 2, both the spacer and the sealing rings were 3D-printed from the same filament as for Prototype 1. In Prototype 3, both spacer and sealing rings were 3D-printed of flexible filament with density of 1.7 kg/m^3 and hardness of 61 Shore D.

IV. Sample Holder Hermitization Estimation

To be able to couple the sample holder to a wide variety of research and assembly setups [31], [39], especially those equipped with compact vacuum pumps with low performance, it is instrumental to evaluate the equivalent area of the slits, holes and airgaps, the existence of which result in pressure losses, which, in turns, results in the reduce in holding force. The holding force can be used not only to hold the component and prevent its misalignment, but also to minimize the warpage [32]. The information on airgaps area is needed for design and setting the proper parameters of the vacuum system.

The known methods of evaluating the equivalent slit area of the housing, which are based on the pressure step change transient analysis [54], should be adapted for the implementation

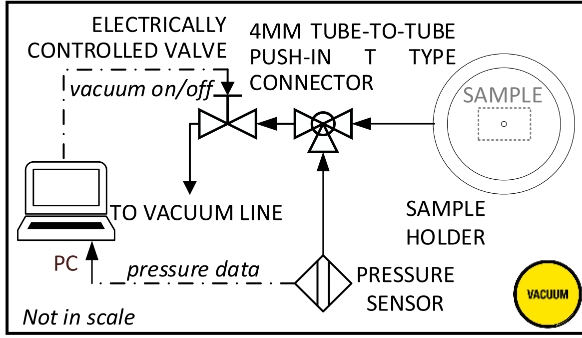

Fig. 5. Sample holder air leakage measuring setup.

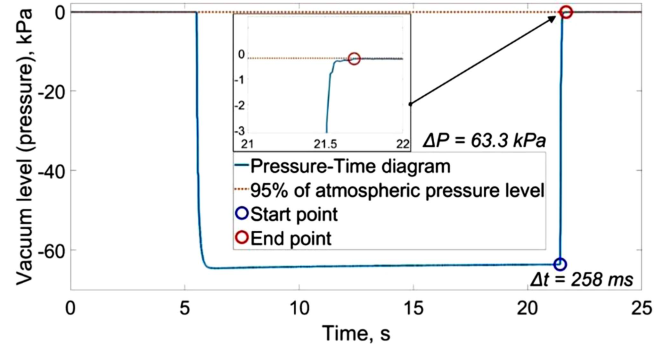

Fig. 6. Example of transient plot for prototype 1 of vacuum sample holder.

with the proposed vacuum holder design, as it has a low value of the internal cavity volume ($\sim$12 cm^3) and a low expected value of slit area due to the design and the usage of sealing rings. For this purpose, it is necessary to investigate the transient process (i.e., when the vacuum source is rapidly turned off), since the equalization of pressure to the atmospheric level is achieved due to the existing slits, holes, and airgaps of the design. The equivalent hole area S_h can be evaluated using the following equation:

$$S_h = k\left(\frac{V_c \Delta P_{pa}}{\Delta t} - b\right) \tag{3}$$

where V_c – is the cavity volume (m^3), ΔP_{pa} – is the pressure difference between the start and end points of the transient (Pa),

Δt – is the transient time (s), k – is a proportionality factor, which is individual for each design due to the variations of the internal cavity volumes and different leakage levels, b – is the leakage, which is not related to the sample holder (system eigen background leakage). Due to pressure level oscillations, which occur in the final stage of the transition, 95% of the atmospheric pressure level is chosen as the end point of the transition [54].

As the prototypes have identical and known vacuum holes configurations (1 mm diameter in the center of top transparent layer, which corresponds to S_{vh} area of 0.785 mm^2), the proportionality factor k for each prototype may be calculated as the difference in the equivalent hole area between the prototype with open and blocked vacuum hole, according to equation:

$$k = S_{vh} / \left(\left[\frac{V_c \Delta P_{pa}}{\Delta t}\right]_{open} - \left[\frac{V_c \Delta P_{pa}}{\Delta t}\right]_{closed}\right) \tag{4}$$

The scheme of the measuring setup is presented in Fig. 5. The experiment was carried out as follows: the prototype with a blocked vacuum hole was connected to a vacuum line with a 4 mm vacuum hose. The vacuum line on-off state was controlled with an electronically switchable valve, which was connected to a computer (PC). The pressure level in the line was continuously monitored with a digital pressure sensor with sampling rate of 1 kHz. The valve was then switched to the active state (vacuum on).

After holding it in active state for $\sim$20 seconds, it was switched to the passive state (vacuum off), triggering the desired transient process. After carrying out such a leakage measurements multiple times to account for random errors, the vacuum hole was blocked with a sample [40], [55], [56] and measurements were taken again.

An example of a transient plot for Prototype 1 with closed vacuum hole is presented in Fig. 6 (vacuum level of $\sim$0 kPa corresponds to the atmospheric pressure level). The measurement of system eigen leakage level b is proceeded in the same manner, but with hermetically sealed test sample with cavity volume V_c of $\sim$1.3 cm^3 connected instead of sample holder prototype. Then, the proportionality factor k can be easily calculated, from which the equivalent hole area for each prototype could be found.

The experimental data is presented in Table I. The proportionality factor k is different for each of the investigated prototypes. The equivalent hole area is 0.254, 7.032 and 3.786 mm^2 for Prototypes 1–3, respectively. This could be virtually described as two uniform slits with heights about 1.2, 31.1 and 16.7 μm for Prototypes 1–3, respectively, around the outer perimeters of both surfaces of transparent layers, which looks realistic. This is a theoretical representation, based on the assumption, that transparent layers and sealing rigs of a sample holder have the uniform gaps with diameters corresponding to the outer diameters of transparent layers and areas, equal to the equivalent hole area of each prototype. This evaluation has been added as an additional sanity check for the proposed hermitization estimation method.

For further reference, the same measurement approach was tested on a commercially available 4 × 2” gel box vacuum release (VR) tray (non-transparent, non-reconfigurable stainless-steel tray with V_c of $\sim$3.5 cm^3 and 4x3 mm diameter vacuum holes, closed by 4 of 2” gel boxes). The equivalent hole area for the gel box tray is 6.776 mm^2. The measurement results indicate that the proposed sample holder design has performance level, comparable to the industrial grade vacuum devices. The difference in the proportionality factor values between the proposed sample holder and gel box tray is defined by the difference in structure: the volume of the internal cavity differs by more than three times, and the total area of the vacuum holes - by more than thirty times, which significantly affects the dynamics of transient processes.

Despite the differences in air leakage values, all prototypes were able to hold the PIC sample in position by vacuum force

TABLE I
EXPERIMENTAL DATA FOR VACUUM SAMPLE HOLDER HERMITIZATION ESTIMATION

Sample under test	*Vacuum hole status*	*Measurement 1*	*Measurement 2*	*Measurement 3*	*Average value*	*Proportionality factor, k*	*Equivalent hole area, mm²*
Eigen leakage test, *b*	closed (sealed)	0.441	0.807	0.378	0.542	–	–
Gel box vacuum release tray (stainless steel)	open	2.419	1.175	1.191	1.595	20.418	6.776
	closed	0.210	0.211	0.209	0.210		
Prototype 1 (1.6 kg/m³, 98 ShA + 0.8 mm 72 ShM)	open	9.869	9.547	9.598	9.671	0.114	0.254
	closed	2.678	2.654	2.996	2.716		
Prototype 2 (1.6 kg/m³, 98 ShA)	open	15.721	15.001	14.752	15.158	0.535	7.032
	closed	13.623	13.059	14.388	13.690		
Prototype 3 (1.7 kg/m³, 61 ShD)	open	10.848	6.715	9.837	9.133	0.532	3.786
	closed	6.259	7.352	9.363	7.658		

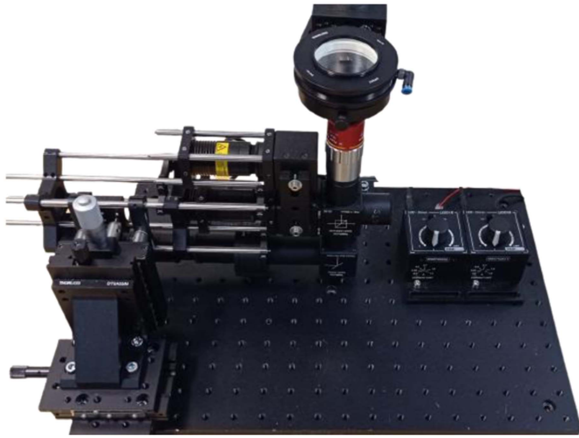

Fig. 7. The prototype of proposed sample holder design used together with *bSi*-based IR microscope prototype for through-silicon vision [40].

during complete 180° flipping of the sample holder along the *X* and *Y* axes (*Rx* and *Ry* according to the coordinate system in Fig. 1), and were tolerant to moderate accelerations and shocks, occurring during normal operation of research and assembly setups, including the usage of pick-up tools [31], [39].

The hermitization degree may be significantly increased by using different types of sealing compounds, but in this case the key feature of the proposed design – the possibility of changing the configuration of vacuum holes and desired transmission by replacing the transparent layers – is not available. An intermediate solution may include the use of sealing tapes.

V. SAMPLE HOLDER IMPLEMENTATION FOR THROUGH-SILICON MICROSCOPY AND LASER-ASSISTED BONDING

The Fig. 7 shows the prototype of proposed sample holder design implemented together with *bSi*-based IR microscope for through-silicon vision [40]. As the test target we used elements № 6 of group 7 of positive and negative USAF 1951 (United States Air Forces MIL-STD-150A 1951 standard) having a 2.19 μm width. An average contrast increase from 5.3% to 10.5% was obtained compared to PMMA-based sample holder both for sagittal and tangential orientation [40]. The contrast of images along the center line of the component increased from 19% to above 22% for the single-layered PIC (Fig. 8(a)), from

12% to above 20% for the bottom (Fig. 8(b)) and from 8% to above 14% for the top (Fig. 8(c)) layer of the double-layered PIC [40], [55], [56], compared to the PMMA-based sample holder

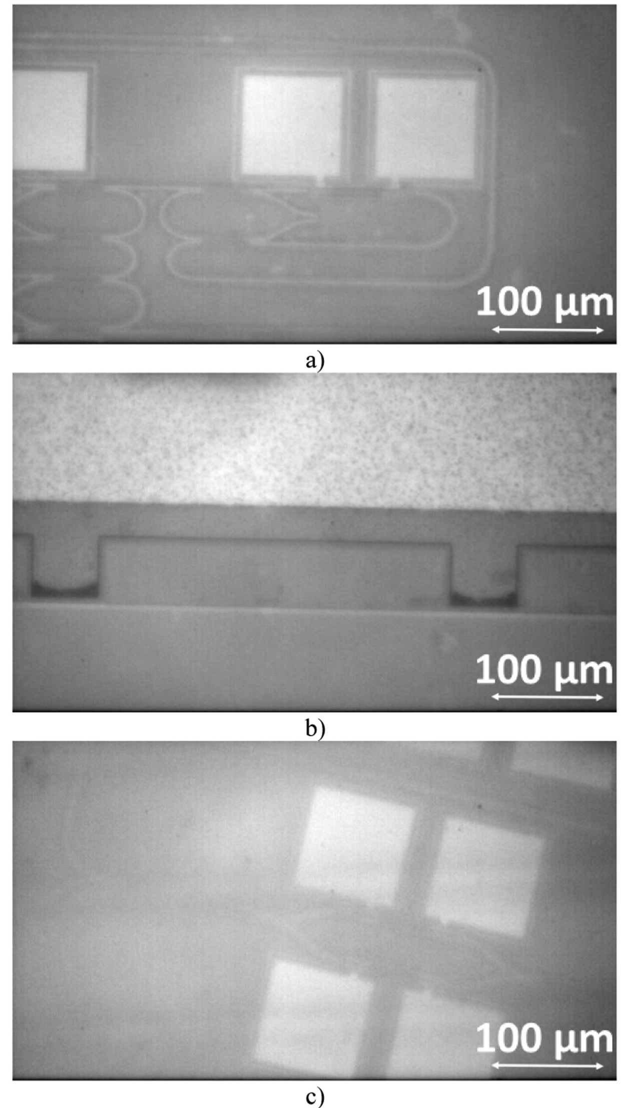

Fig. 8. The through-silicon images, taken with IR microscope [40] using the proposed sample holder design: (a)-Single-layered PIC, (b)-bottom layer of double-layered stacked PIC structure, (c)-top layer of double-layered stacked PIC structure.

case [40], [57]. The through-silicon images were taken under the same conditions, their contrast and modulation transfer function (MTF, [40], [57]) were evaluated in the same manner as for PMMA-based sample holder case [40] to get fully comparable results. The contrast rate of each image was evaluated according

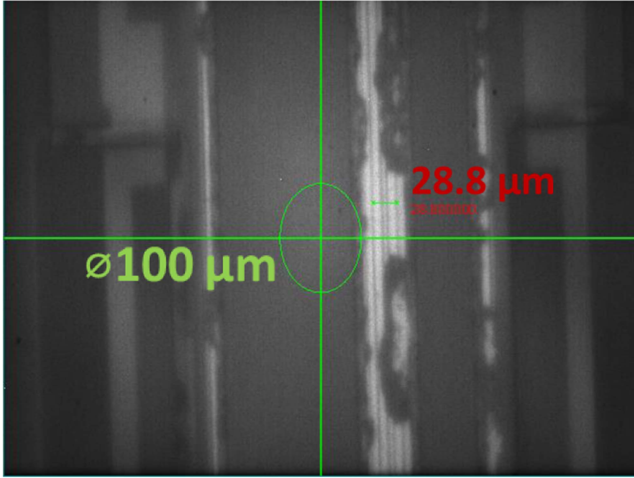

Fig. 9. Through-silicon III/V-chip-to-PIC placement error estimation.

to the following equation [40], [57]:

$$Contrast\ (\%) = \frac{(I_{\max} - I_{\min})}{(I_{\max} + I_{\min})} \cdot 100\% \qquad (5)$$

where $I_{\max}$ – is the image maximum brightness value (digits) and $I_{\min}$ – is the image minimum brightness value (digits).

Furthermore, the proposed sample holder was used for the through-silicon III/V-chip-to-PIC placement error estimation and flip-chip alignment (according to the Figs. 1(c) and 7). From Fig. 9, it is seen that initial chip-to-PIC waveguide-to-waveguide placement error was near 28.8 μm, which subsequently was corrected by the pick-up tool movement during through-silicon alignment.

Finally, the proposed sample holder was tested during the proof-of-concept for a custom LAB prototype equipment, consisting of 980 nm laser bottom irradiation beam delivery system [58], [59], [60]. The test PIC [40], [55], [56] with 100 × 100 μm *Au*-plated pads, covered with a pre-dispensed type 619D solder paste (*Sn62/Pb36/Ag2*, metal content 86%, mesh type 3) was placed on the proposed sample holder accordingly to the Fig. 1(c). During the test, two irradiation modes with the power densities of 240 and 110 W/cm^2 at 980 nm and uniform "top-hat" beam profile are investigated. These irradiation modes were chosen as two boundary cases with significantly different dynamics of the thermal process – "fast" and "slow" correspondingly. To ensure solder melting and proper bonding, a target temperature of 300 °C was chosen. The in-situ temperature control was performed using non-contact pyrometer. The time-temperature diagrams (so-called "shark fins") of a 3 mm diameter central spot on the PIC top surface are presented in Fig. 10, and the microscope, IR-visualizer and thermal imager photos of the sample are given in Fig. 11. Both LAB operation modes resulted in the heating of the PIC above the solder melting temperature, which in turns led to the successful bond formation with electrical impedance in the range of hundredths of an Ohm, which is consistent with the published data [33].

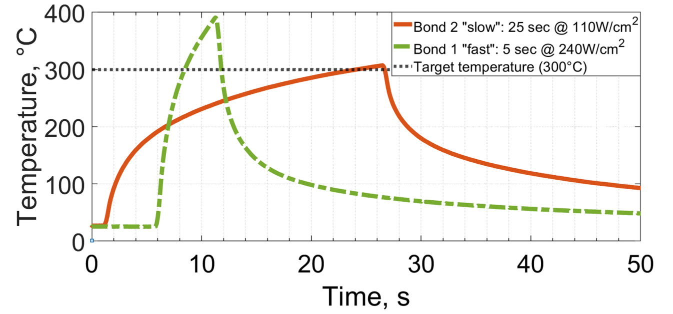

Fig. 10. Time-temperature diagrams ("shark fins") of the LAB process.

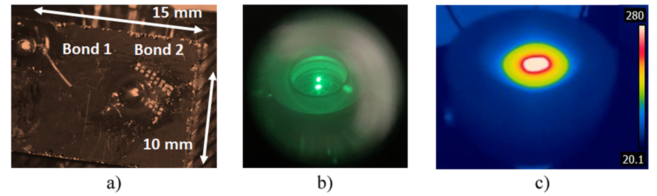

Fig. 11. Microscope (a), IR-visualizer (b), and thermal imager (c) photos of the test sample, taken during test LAB process.

Furthermore, based on the thermal image (Fig. 11) captured during the LAB process, it can be concluded that the transparent layers and AR coatings primarily confine the thermal field inside the test sample, causing only slight heating of the surrounding transparent layer due to thermal contact. This indicates that the proposed design of the sample holder achieves a high efficiency in converting light to heat.

Thus, the implementation of the proposed sample holder design significantly improves the performance of IR through-silicon imaging system due to optical properties of transparent layers and AR coatings. The proposed sample holder design is validated for photonic integration assembly processes.

VI. Conclusion

A simple, reliable, and cost-effective reconfigurable vacuum sample holder design concept tailorable for flexible LAB processes was demonstrated. The holder is compatible with electronic and photonic integration LAB processes, as well as with IR through-silicon microscopy applications with top and bottom irradiation (illumination) architectures. These aspects make this concept instrumental for a large variety of research, assembly, lithography, and wafer bonding setups. The proposed design has a high hermitization degree and can be used in through-silicon IR microscopy. Its implementation significantly improves the performance of IR through-silicon imaging system owing to optical properties of transparent layers and AR coatings.

The proposed principle of construction can be taken as the basis of a sample holder designs for large diameter wafer-level integration processes. Also, the proposed method of evaluating the equivalent slit area can be used for design and setting the proper parameters of a vacuum system, as well as for investigation and comparative study of different design options.

References

[1] T. Barnett et al., "Cisco visual networking index (VNI) complete forecast update, 2017–2022," *Amer./EMEAR Cisco Knowl. Netw. Presentation*, pp. 1–30, 2018. Accessed: Dec. 24, 2022. [Online]. Available: https://www.cisco.com/c/dam/m/en_us/network-intelligence/service-provider/digital-transformation/knowledge-network-webinars/pdfs/1213-business-services-ckn.pdf

[2] "Mobile traffic 2022 Q3 update-mobility report," 2022. Accessed: Dec. 24, 2022. [Online]. Available: https://www.ericsson.com/en/reports-and-papers/mobilityreport/dataforecasts/mobile-traffic-update#:∼:text=Mobile%20network%20data%20traffic%20grew

[3] J. H. Lau, "Recent advances and trends in advanced packaging," *IEEE Trans. Compon., Packag. Manuf. Technol.*, vol. 12, no. 2, pp. 228–252, Feb. 2022, doi: 10.1109/tcpmt.2022.3144461.

[4] P. Kaur et al., "Hybrid and heterogeneous photonic integration," *Appl. Phys. Lett. Photon.*, vol. 6, no. 6, Jun. 2021, Art. no. 061102, doi: 10.1063/5.0052700.

[5] N. Margalit et al., "Perspective on the future of silicon photonics and electronics," *Appl. Phys. Lett.*, vol. 118, no. 22, May 2021, Art. no. 220501, doi: 10.1063/5.0050117.

[6] D. Liang and J. E. Bowers, "Recent progress in heterogeneous III-V-on-silicon photonic integration," *Light: Adv. Manuf.*, vol. 2, no. 1, pp. 1–25, 2021, doi: 10.37188/lam.2021.005.

[7] B. Corbett et al., "Transfer print techniques for heterogeneous integration of photonic components," *Prog. Quantum Electron.*, vol. 52, pp. 1–17, Mar. 2017, doi: 10.1016/j.pquantelec.2017.01.001.

[8] N. Lindenmann et al., "Photonic wire bonding: A novel concept for chip-scale interconnects," *Opt. Exp.*, vol. 20, no. 16, pp. 17667–17677, Jul. 2012, doi: 10.1364/oe.20.017667.

[9] M. Theurer et al., "Flip-chip integration of *InP* to *SiN* photonic integrated circuits," *J. Lightw. Technol.*, vol. 38, no. 9, pp. 2630–2636, May 2020, doi: 10.1109/jlt.2020.2972065.

[10] N. Zia et al., "Hybrid silicon photonics DBR laser based on flip-chip integration of *GaSb* amplifiers and μm-scale SOI waveguides," *Opt. Exp.*, vol. 30, no. 14, pp. 24995–25005, Jun. 2022, doi: 10.1364/oe.460883.

[11] L. Granados et al., "Silicate glass-to-glass hermetic bonding for encapsulation of next-generation optoelectronics: A review," *Mater. Today*, vol. 47, pp. 131–155, Jul. 2021, doi: 10.1016/j.mattod.2021.01.025.

[12] A. Mohan et al., "A wafer-level packaging approach for MEMS and related microsystems using selective laser-assisted bonding (LAB)," in *Proc. Electron. Compon. Technol.*, 2005, pp. 1099–1102a, doi: 10.1109/ECTC.2005.1441409.

[13] R. Witte et al., "Microjoining of dissimilar materials for optoelectronic and biomedical applications," *Proc. SPIE*, vol. 4979, pp. 226–233, 2003, doi: 10.1117/12.478282.

[14] G. D. Liu, C. Wang, and J. Swingler, "Laser-assisted sintering of silver nanoparticle paste for bonding of silicon to DBC for high-temperature electronics packaging," *IEEE Trans. Compon., Packag. Manuf. Technol.*, vol. 11, no. 3, pp. 522–529, Mar. 2021, doi: 10.1109/TCPMT.2020.3046917.

[15] H. H. Busta et al., "Attachment of optoelectronic components to silicon submounts by Nd:YAG laser soldering of indium," *J. Micromechanics Microengineering*, vol. 4, no. 3, pp. 110–115, Sep. 1994, doi: 10.1088/0960-1317/4/3/003.

[16] A. W. Y. Tan and F. E. H. Tay, "Localized laser assisted eutectic bonding of quartz and silicon by Nd:YAG pulsed-laser," *Sensors Actuators A: Phys.*, vol. 120, no. 2, pp. 550–561, May 2005, doi: 10.1016/j.sna.2004.11.035.

[17] A. E. Aydin et al., "Numerical simulation of selective laser-assisted bonding (LAB) process for photonic integration," 2022. Accessed: Dec. 24, 2022. [Online]. Available: https://www.researchgate.net/publication/364039899_Numerical_Simulation_of_Selective_Laser-Assisted_Bonding_LAB_Process_for_Photonic_Integration

[18] K.-S. Choi et al., "Interconnection process using laser and hybrid underfill for LED array module on PET substrate," in *Proc. IEEE 68th Electron. Compon. Technol. Conf.*, 2018, pp. 1567–1573, doi: 10.1109/ECTC.2018.00238.

[19] K.-S. Choi et al., "Development of digital signage modules composed of mini-LEDs using laser-assisted bonding (LAB) technology," in *Proc. IEEE 70th Electron. Compon. Technol. Conf.*, 2020, pp. 1031–1036, doi: 10.1109/ECTC32862.2020.00167.

[20] W. A. Braganca and K. Kim, "Characterization of laser beams: Theory and application in laser-assisted bonding process," *Proc. SPIE*, vol. 60, no. 6, Jun. 2021, Art. no. 060801, doi: 10.1117/1.oe.60.6.060801.

[21] Y. Jung et al., "Development of next generation flip chip interconnection technology using homogenized laser-assisted bonding," in *Proc. IEEE 66th Electron. Compon. Technol. Conf.*, 2016, pp. 88–94, doi: 10.1109/ECTC.2016.76.

[22] W. A. Braganca, K. KyungOe, and K. YoungCheol, "Development of a laser-assisted bonding process for a flip-chip die with backside metallization," in *Proc. IEEE 22nd Electron. Packag. Technol. Conf.*, 2020, pp. 68–72, doi: 10.1109/EPTC50525.2020.9315012.

[23] A. Kolbasow, T. Kubsch, M. Fettke, G. Friedrich, and T. Teutsch, "Vertical laser assisted bonding for advanced '3.5D' chip packaging," in *Proc. IEEE 69th Electron. Compon. Technol. Conf.*, 2019, pp. 210–217, doi: 10.1109/ECTC.2019.00039.

[24] M. Fettke, T. Kubsch, A. Kolbasow, V. Bejugam, A. Frick, and T. Teutsch, "Laser-assisted bonding (LAB) and de-bonding (LAdB) as an advanced process solution for selective repair of 3D and multi-die chip packages," in *Proc. IEEE 70th Electron. Compon. Technol. Conf.*, 2020, pp. 1016–1024, doi: 10.1109/ECTC32862.2020.00165.

[25] M. Fettke et al., "A study on laser-assisted bonding (LAB) and its influence on luminescence characteristics of blue and *YAG* phosphor encapsulated *InGaN* LEDs," in *Proc. IEEE 70th Electron. Compon. Technol. Conf.*, 2020, pp. 1928–1934, doi: 10.1109/ectc32862.2020.00301.

[26] M. Gim, C. Kim, S. Na, D. Ryu, K. Park, and J. Kim, "High-performance flip chip bonding mechanism study with laser assisted bonding," in *Proc. IEEE 70th Electron. Compon. Technol. Conf.*, 2020, pp. 1025–1030, doi: 10.1109/ECTC32862.2020.00166.

[27] C. Kim et al., "Development of extremely thin profile flip chip CSP using laser assisted bonding technology," in *Proc. IEEE Compon., Packag. Manuf. Technol. Symp. Jpn.*, 2017, pp. 45–49, doi: 10.1109/ICSJ.2017.8240085.

[28] K.-S. Choi et al., "Laser-assisted bonding (LAB), its bonding materials, and their applications," *J. Weld. Joining*, vol. 38, no. 2, pp. 138–144, Apr. 2020, doi: 10.5781/jwj.2020.38.2.2.

[29] Y. M. Jang et al., "Development and optimization of the laser-assisted bonding process for a flip chip package," *Microsystem Technol.*, vol. 26, no. 3, pp. 1043–1054, Sep. 2019, doi: 10.1007/s00542-019-04624-8.

[30] W. A. Braganca et al., "Collective laser-assisted bonding process for 3D TSV integration with NCP," *Electron. Telecommun. Res. Inst. J.*, vol. 41, no. 3, pp. 396–407, Apr. 2019, doi: 10.4218/etrij.2018-0171.

[31] "FiconTEC webinars–ficonTEC service (sub-μm through-silicon alignment)," *ficonTEC*, 2021. Accessed: Dec. 24, 2022. [Online]. Available: https://www.ficontec.com/webinar/

[32] S. Na et al., "Next gen laser assisted bonding (LAB) technology," in *Proc. IEEE 72nd Electron. Compon. Technol. Conf.*, 2022, pp. 1991–1995, doi: 10.1109/ectc51906.2022.00313.

[33] J. Joo, Y.-S. Eom, K. Jang, G.-M. Choi, and K.-S. Choi, "Development of bonding process for flexible devices with fine-pitch interconnection using anisotropic solder paste and laser-assisted bonding technology," in *Proc. IEEE 70th Electron. Compon. Technol. Conf.*, 2020, pp. 1309–1314, doi: 10.1109/ECTC32862.2020.00207.

[34] C.-Y. Chen, I. Hsu, S. Lin, D. Park, and M.-C. Hsieh, "Laser assisted bonding technology enabling fine bump pitch in flip chip package assembly," in *Proc. 7th Electron. Syst.-Integration Technol. Conf.*, 2018, pp. 1–6, doi: 10.1109/ESTC.2018.8546345.

[35] S. Bao et al., "A review of silicon-based wafer bonding processes, an approach to realize the monolithic integration of Si-CMOS and III–V-on-Si wafers," *J. Semicond.*, vol. 42, no. 2, Feb. 2021, Art. no. 023106, doi: 10.1088/1674-4926/42/2/023106.

[36] J.-W. Nah, Y. Martin, S. Kamlapurkar, S. Engelmann, R. L. Bruce, and T. Barwicz, "Flip chip assembly with sub-micron 3D re-alignment via solder surface tension," in *Proc. IEEE 65th Electron. Compon. Technol. Conf.*, 2015, pp. 35–40, doi: 10.1109/ECTC.2015.7159568.

[37] Y. Martin, J.-W. Nah, S. Kamlapurkar, S. Engelmann, and T. Barwicz, "Toward high-yield 3D self-alignment of flip-chip assemblies via solder surface tension," in *Proc. IEEE 66th Electron. Compon. Technol. Conf.*, 2016, pp. 588–594, doi: 10.1109/ECTC.2016.239.

[38] D. Hobbs et al., "Astro2020 activity, project of state of the profession consideration (APC) white paper: All-sky near infrared space astrometry. State of the profession considerations: Development of scanning NIR detectors for astronomy," 2019, *arXiv:1907.05191*.

[39] G. Böttger et al., "Fully automated hybrid diode laser assembly using high precision active alignment," *Proc. SPIE*, vol. 9730, Apr. 2016, Art. no. 97300E, doi: 10.1117/12.2214718.

[40] A. A. Vlasov, A. E. Aydin, T. Uusitalo, J. Viheriälä, and M. Guina, “Machine vision system utilizing black silicon CMOS camera for through-silicon alignment,” *IEEE Trans. Compon., Packag. Manuf. Technol.*, vol. 12, no. 12, pp. 2019–2026, Dec. 2022, doi: 10.1109/TCPMT.2022.3225051.

[41] U. Gengenbach et al., “Automated fabrication of hybrid printed electronic circuits,” *Mechatronics*, vol. 70, Oct. 2020, Art. no. 102403, doi: 10.1016/j.mechatronics.2020.102403.

[42] D. W. Grund, G. A. Ejzak, G. J. Schneider, J. Murakowski, and D. W. Prather, “A widely tunable narrow linewidth RF source integrated in a heterogeneous photonic module,” *J. Lightw. Technol.*, vol. 32, no. 7, pp. 1363–1369, Apr. 2014, doi: 10.1109/jlt.2014.2302138.

[43] H. Lu et al., “Flip-chip integration of tilted VCSELs onto a silicon photonic integrated circuit,” *Opt. Exp.*, vol. 24, no. 15, Jul. 2016, Art. no. 16258, doi: 10.1364/oe.24.016258.

[44] A. Moel, “A compact, low-cost system for sub-100 nm X-ray lithography,” *J. Vac. Sci. Technol. B: Microelectronics Nanometer Struct.*, vol. 8, no. 6, Nov. 1990, Art. no. 1648, doi: 10.1116/1.585133.

[45] B. Snyder, B. Corbett, and P. O’Brien, “Hybrid integration of the wavelength-tunable laser with a silicon photonic integrated circuit,” *J. Lightw. Technol.*, vol. 31, no. 24, pp. 3934–3942, Dec. 2013, doi: 10.1109/jlt.2013.2276740.

[46] N. Hiromoto et al., “Precise and convenient reflection THz-time domain spectroscopy with a movable transparent sample holder,” in *Proc. IEEE 38th Int. Conf. Infrared, Millimeter, Terahertz Waves*, 2013, pp. 1–2, doi: 10.1109/IRMMW-THz.2013.6665509.

[47] D. W. Grund et al., “Integrated silicon-photonic module for generating widely tunable, narrow-line RF using injection-locked lasers,” *Proc. SPIE*, vol. 8259, 2012, Art. no. 825906, doi: 10.1117/12.914467.

[48] D. W. Grund, G. A. Ejzak, G. J. Schneider, J. Murakowski, and D. W. Prather, “Heterogenous integrated silicon-photonic module for producing widely tunable narrow linewidth RF,” in *Proc. IEEE Int. Topical Meeting Microw. Photon.*, 2013, pp. 100–103, doi: 10.1109/MWP.2013.6724029.

[49] A. Sojka et al., “Sample holders for sub-THz electron spin resonance spectroscopy,” *IEEE Trans. Instrum. Meas.*, vol. 71, 2022, Art. no. 8002812, doi: 10.1109/tim.2022.3164135.

[50] M. Okano et al., “Vibration isolation for scanning tunneling microscopy,” *J. Vac. Sci. Technol. Vac., Surfaces, Films*, vol. 5, no. 6, pp. 3313–3320, 1987.

[51] A. A. Vlasov et al., “Development of the passive vibroacoustic isolation system for the path matched differential interferometry based fiber-optic sensors,” *Opt. Fiber Technol.*, vol. 57, Jul. 2020, Art. no. 102241, doi: 10.1016/j.yofte.2020.102241.

[52] “The model for calculating the frictional moment,” 2006. Accessed: Dec. 24, 2022. [Online]. Available: https://www.skf.com/binaries/pub12/Images/0901d1968065e9e7-The-SKF-model-for-calculating-the-frictional-moment_tcm_12-299767.pdf

[53] S. Nisar et al., “Laser glass cutting techniques—A review,” *J. Laser Appl.*, vol. 25, no. 4, Aug. 2013, Art. no. 042010, doi: 10.2351/1.4807895.

[54] A. A. Vlasov et al., “Research on the influence of the degree of acoustic sealing of acoustically conditioned sound protective cases of fiber-optic interferometers on their characteristics,” *Instrum. Exp. Techn.*, vol. 63, no. 4, pp. 502–506, Jul. 2020, doi: 10.1134/s0020441220040351.

[55] T. Aalto et al., “Open-access 3-μm *SOI* waveguide platform for dense photonic integrated circuits,” *IEEE J. Sel. Topics Quantum Electron.*, vol. 25, no. 5, Sep./Oct. 2019, Art. no. 8201109, doi: 10.1109/jstqe.2019.2908551.

[56] S.-P. Ojanen et al., “GaSb diode lasers tunable around 2.6 μm using silicon photonics resonators or external diffractive gratings,” *Appl. Phys. Lett.*, vol. 116, no. 8, Feb. 2020, Art. no. 081105, doi: 10.1063/1.5140062.

[57] N. Menn, *Practical Optics*. Amsterdam, The Netherlands: Elsevier, 2004.

[58] A. A. Vlasov et al., “Laser-assisted bonding approach for photonic integration processes,” in *Proc. 24th Eur. Microelectronics Packag. Conf.*, 2023.

[59] A. A. Vlasov et al., “Laser-assisted bonding prototype equipment for hybrid integration of silicon photonic circuits,” in *Proc. Conf. Laser Electro-Opt./Europe-Eur. Quantum Electron. Conf.*, 2023.

[60] A. A. Vlasov et al., “Laser-assisted bonding prototype equipment for hybrid integration of silicon photonic circuits,” 2023. Accessed: Jul. 07, 2023. [Online]. Available: https://www.researchgate.net/publication/372078309_Laser-Assisted_Bonding_Prototype_Equipment_for_Hybrid_Integration_of_Silicon_Photonic_Circuits